Solid State Ionics 368 (2021) 115639

Contents lists available at ScienceDirect

Solid State Ionics

journal homepage: www.elsevier.com/locate/ssi

Oxygen exchange and bulk diffusivity of $BaCo_{0.4}Fe_{0.4}Zr_{0.1}Y_{0.1}O_{3-\delta}$: Quantitative assessment of active cathode material for protonic ceramic fuel cells

Yuqing Meng [a], Jack Duffy [a], Beom Tak Na [b], Jun Gao [a], Tao Yang [b,c], Jianhua Tong [a], Shiwoo Lee [b,c], Kyle S. Brinkman [a,*]

[a] Department of Materials Science and Engineering, Clemson University, Clemson, SC 29634, USA
[b] National Energy Technology Laboratory, Morgantown, WV 26505, USA
[c] Leidos Research Support Team, Morgantown, WV 26505, USA

A B S T R A C T

The oxygen surface exchange and bulk diffusivity of $BaCo_{0.4}Fe_{0.4}Zr_{0.1}Y_{0.1}O_{3-\delta}$ were determined by electrical conductivity relaxation (ECR) in order to quantitively assess cathode performance for protonic ceramic fuel cells (PCFCs). The measurements were performed at 600 °C, following pO_2-step changes between 80 ppm to pure oxygen. The apparent value of surface exchange coefficient (k) and diffusion coefficient D, indicates $BaCo_{0.4}Fe_{0.4}Zr_{0.1}Y_{0.1}O_{3-\delta}$ is a good oxygen conductor. k was found to vary with pO_2 and surface area while the chemical diffusion coefficient D remained invariant with pO_2 and surface coating. The fitted kinetic parameters obtained from ECR with reduction process (high to low pO_2) were compared with that of the oxidation process (low to high pO_2). In the presence of H_2O, oxygen exchange kinetics was suppressed because of the competitive adsorption relationship between oxygen and H_2O. Single cell measurements employing single phase $BaCo_{0.4}Fe_{0.4}Zr_{0.1}Y_{0.1}O_{3-\delta}$ cathode and an anode prepared by phase inversion tape casting in a configuration of 40 wt% BCZYSm13 + 60 wt% NiO | BCZYSm13 | BCFZY0.1 exhibited a power density of ~200 mW/cm^2 at 600 °C.

1. Introduction

Protonic conducting fuel cells (PCFCs) are an emerging sub-class of solid oxide fuel cells (SOFCs) with great potential for lowering the operating temperature to the range of 400–600 °C. [1] PCFC are electrochemical conversion devices that produces electricity by oxidizing a fuel such as hydrogen or hydrocarbons [2]which can achieve higher fuel utilization due to the generation of water on the cathode side, effectively avoiding the dilution of the fuel gas.

Proton conducting electrolyte materials, many of which are perovskite-structured, offer high ionic conductivity with a low electronic transport number. [3–7] As one of the state-of-art electrolytes for PCFC, $BaZr_{0.1}Ce_{0.7}Y_{0.2}O_{3-\delta}$ (BZCY) [8,9]has received great attention in recent reports. Yang et al. reported Yb-doped BZCY exhibits high ionic conductivity and enhanced water adsorption capability. [3] However, the high refractory nature of Yb-doped BZCY limit the fabrication and processing of PCFCs to next level. Recently, Sm-doped BCZY was found to have improved sinterability with large grain size features. [10]

The cathode of PCFC plays a key role in determining the overall cell performance. [11] The transport of oxygen ions, protons and electrons are all crucial for the cathode performance. Recently, a triple conducting (proton, oxygen ion and electron hole) $BaCo_{0.4}Fe_{0.4}Zr_{0.1}Y_{0.1}O_{3-\delta}$ (BCFZY0.1) was developed and shown to be a highly active and chemically stable cathode material, [1] which demonstrated improved oxygen reduction reaction (ORR) kinetics at intermediate temperatures. The triple conducting feature of BCFZY0.1 makes the entire cathode surface electrochemically active, eliminating the triple-phase boundary constraints often present in traditional composite cathode architectures. Chen et al. [12] found that the proton uptake reaction rate of BCFZY0.1 can be enhanced by coating $Sm_{0.2}Ce_{0.8}O_{1.9}$ (SDC) nanoparticles, indicating proton uptake in BCFZY0.1 is a surface exchange limiting process. Water uptake capacity is also important for PCFC cathode materials. Several factors, such as the oxide-ion basicity, the oxidation state of B-site cations and the B—O covalency, can determine the proton concentration. Proton uptake in BCFZY0.1 was detected by TGA and the proton concentration at 250 °C and 16 mbar H_2O was calculated to be 2.2 mol %. [13] Ren et al. introduced A-site deficient to tune the triple-conducting properties, and a remarkable performance was obtained on $Ba_{0.9}Co_{0.4}Fe_{0.4}Zr_{0.1}Y_{0.1}O_{3-\delta}$, with a peak power density of 668 mW/cm^2 was obtained at 600 °C. [14] Kuai et al. reported that a significantly

* Corresponding author.
E-mail address: ksbrink@clemson.edu (K.S. Brinkman).

https://doi.org/10.1016/j.ssi.2021.115639
Received 2 November 2020; Received in revised form 18 March 2021; Accepted 16 April 2021

improved ORR activity was observed by introducing a slight B-site cation deficiency. [15] $Ba(Co_{0.4}Fe_{0.4}Zr_{0.1}Y_{0.1})_{0.975}O_{3-\delta}$ shows an area specific resistance of 0.011 Ω/cm^2 at 600 °C. A similar result was found by Li et al. when BCFZY0.1 was used as electrocatalysts for hydrogen evolution reaction (HER). [16] Recently, it was demonstrated that a BCFZY0.1 cathode exfoliated BCFZY0.1 nanoparticles when treated at temperature above 800 °C, [17] resulting in a hierarchical cathode with which the single cell renders a power output of 1.61 W/cm^2 at 700 °C. These results show that BCFZY0.1 is a promising cathode for PCFCs. However, the fundamental material transport properties of oxygen reduction kinetics including surface exchange coefficient *(k),* and diffusion coefficient *(D)* of BCFZY0.1 have not been evaluated for use in quantitatively optimizing cathode performance.

The cathode reaction in PCFCs starts with oxygen adsorptive dissociation on the surface. A higher oxygen adsorption rate for oxygen and a lower energy barrier for oxygen dissociation is preferred for faster reactions. Surface oxygen vacancies present in the cathode material enable rapid oxygen adsorption and dissociation. Determination of oxygen reduction parameters such as surface exchange coefficient (*k*) and diffusion coefficient (*D*) is critical to reveal the cathode mechanism and further improve the cathode material.

Electrical conductivity relaxation (ECR) and isotope exchange (IE) are two popular experimental methods for oxygen reduction kinetics parameter measurement. ECR is widely used for oxygen reduction kinetic parameters measurement for cathode materials, [18–25]owing to its simplified experiments and reduced operating costs. [24,26] In this work, ECR experiments are performed on bare and coated BCFZY0.1 specimen where sample thicknesses are controlled in the diffusion or mixed regimes. Characteristic thickness of BCFZY0.1 was calculated and compared with typical MIEC materials.

2. Experimental section

2.1. Preparation of phase inversion $BaCe_{0.7}Zr_{0.1}Y_{0.07}Sm_{0.13}O_{3-\delta}$ (BCZYSm13) + NiO anode

An anode consisting of 40 wt% BCZYSm13 + 60% wt% NiO was fabricated by phase inversion tape casting method as previously reported [27]. Anode precursor powder of 40 wt% BCZYSm13 + 60 wt% NiO was prepared by mixing proper amount of of $BaCO_3$, CeO_2, ZrO_2, Y_2O_3, Sm_2O_3, NiO (based on total weigh of oxides) and 20 wt% starch (based on the sum of BCZYSm13 and NiO). The raw precursor mixture was mixed with polyvinylpyrrolidone (PVP) as the dispersant and polyethersulfone (PES) as the binder in *N*-methyl-2-pyrrolidone (NMP) solution (Table 1) and blended using ball-milling process for 24 h. The slurry then was cast onto a Mylar substrate with blade height of 1.6 mm and transferred into water bath for solidification for 12 h *via* the phase inversion process (Fig. 1). This was followed by drying the green tape at room temperature for 12 h.

2.2. Preparation of $BaCo_{0.4}Fe_{0.4}Zr_{0.1}Y_{0.1}O_{3-\delta}$ (BCFZY0.1) precursor powder

BCFZY0.1 precursor powder was prepared by a citric-acid method. Stoichiometric amounts of $Ba(NO_3)_2$ (Alfa Aesar, 99 + %), $Co(NO_3)_2{\cdot}6H_2O$ (Alfa Aesar, >98.0%), $Fe(NO_3)_3{\cdot}9H_2O$ (Alfa Aesar, >98.0%), $ZrO(NO_3)_2$ solution (Sigma-Aldrich, ≥99%) and $Y(NO_3)_3{\cdot}6H_2O$ (Alfa Aesar, 99.9%) were dissolved in deionized water in desired molar ratios, then mixed with citric acid (Sigma-Aldrich, ≥99.5%) with a citric acid/metal-ion ratio of 1.5:1. The pH value was adjusted to approximately 9 by adding $NH_3{\cdot}H_2O$. A dark purple gel was obtained by evaporating the water at 80 °C. The as-obtained gel was dried at 150 °C for 48 h to form a primary powder, which was then fired at 600 °C for 5 h followed by ball milling in 1-butanol for 7 days. The cathode precursor powder was obtained by further drying at 500 °C for 5 h. Paste of cathode precursor was prepared by mixing powder, dispersant (20 wt% solsperse 28,000 in terpinol solution), and binder (5 wt% Heraeus V-600 in terpineol solution) in a weight ratio of 15:3:1 by manually grinding for 45 min in a mortar and pestle.

Table 1
Slurry composition of anode layer.

Materials	(40% BCZYSm13 + 60% NiO) + 20% starch	NMP	PES	PVP	Total	Sold content (%)
Weight (g)	50	26.18	4.60	0.79	81.58	61.3

2.3. Fabrication of symmetrical cells and single cells

Symmetrical cells were fabricated in the electrode | electrolyte | electrode configuration. Pellets of $BaCe_{0.7}Zr_{0.1}Y_{0.07}Sm_{0.13}O_{3-\delta}$ (denote as BCZYSm13) were synthesized by the solid-state reactive sintering (SSRS) method [28,29] from cost-effective raw materials of $BaCO_3$ (Alfa Aesar, 99.8%), CeO_2 (Alfa Aesar, 99.9%), ZrO_2 (Alfa Aesar, 99.7%), Y_2O_3 (Alfa Aesar, 99.9%), Sm_2O_3 (Alfa Aesar, 99.9%) and NiO (Baker Analyzed Reagent, 99.0%). Stoichiometric amounts of $BaCO_3$, ZrO_2, CeO_2, Y_2O_3 and Sm_2O_3 were weighted and added into a Nalgene bottle. 1.0 wt% sintering aid of NiO (based on the total weight of precursor mixture) was added into the above powder mixture. The resulted precursor slurry was ball-milled with ethanol (Carolina, 95%) solvent and 12.5 mm diameter spherical alumina grinding media (Inframat Advanced Materials) for 24 h, then dried at 80 °C for 48 h. Green pellets with a diameter of 19 mm was fabricated by uniaxial pressing under 300 MPa pressure for a dwell of 2 min, then the green pellets were sintered at 1400 °C for 18 h in ambient air. The cathode paste was screen printed on both sides of the polished electrolyte followed by calcine at 900 °C for 5 h. Silver paste and silver wire were attached to the electrode surface to work as current collectors and lead wire.

The anode obtained by phase inversion tape casting was punched from the solidified green tape with a diameter of 3/4 quarter followed by drying at 80 °C for 24 h. Then a thin electrolyte precursor paste layer (20–30 μm after firing) was deposited on top of the green anode electrode using screen-printing, followed by sintering at 1400 °C for 18 h. Sintered half-cell was screen-printed with BCFZY0.1 cathode paste on the electrolyte layer. Then the whole structure was fired at 900 °C for 5 h to form a porous anode | electrolyte | porous cathode single cell. Subsequently, silver paste and silver wire were attached to the electrode surface to act as current collectors.

2.4. Characterization

The phase structure of the as-prepared powders was analyzed by X-ray diffraction (XRD with a diffractometer (X'Pert Pro, Phillips, Netherlands) using Cu/kα radiation (λ = 1.54108 Å), with a scan range of 20–80° and a step size of 0.02°. The microstructure of single cells was examined using scanning electron microscopy (SEM, Hitachi S-4800). The as-fabricated single cells were sealed in an aluminum tube by ceramic bond (989FS Ceramic, Cotronics Corp.), using silver wires as the voltage and current leads on both sides. Symmetrical cells were measured by a Solartron 1260 electrochemical workstation over a range of temperatures 450 °C -650 °C under wet flowing air (through room-temperature water bubbler, 50 mL min^{-1}), using a signal amplitude of 100 mV in the frequency range of 0.01 Hz–5 MHz. The electrochemical performance of single cells was evaluated by using hydrogen as the fuel and synthetic air as oxidant. The flow rates of sweep and feed gases were set to be 30 and 100 mL min^{-1}, respectively.

ECR method was applied to determine the oxygen surface exchange coefficient *k* and diffusion coefficient *D*. The BCFZY0.1 powder was pressed into rectangular bars at a pressure of 300 MPa and sintered at 1260 °C for 8 h in air to form dense pellets. The relative density was

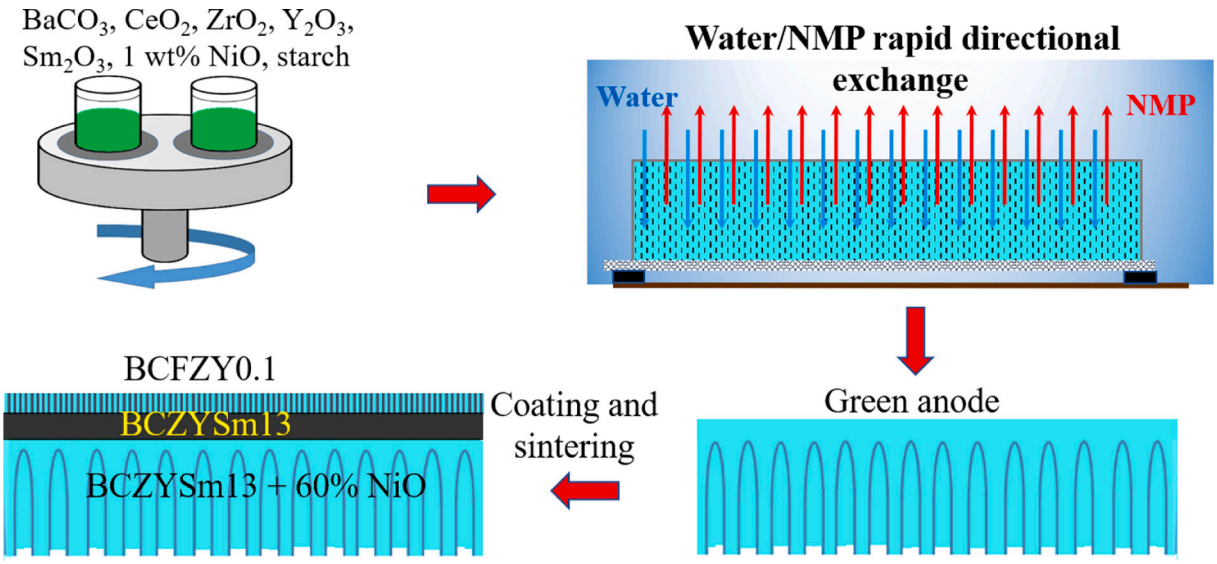

Fig. 1. Fabrication of single cell with 40% BCZYSm13 + 60% NiO anode with phase inversion tape casting technique.

determined to be 96% of the theoretical density using Archimedes method. The sintered bars had dimensions of approximately 11.0 × 5.5 × 1.12 mm^3. To increase the surface area, BCFY0.1 paste was deposited on the surface of rectangular bar (~15 μm after calcining) by screen printing, followed by calcine at 900 °C for 5 h. The conductivity was measured using the four-probe method with a digital multimeter (Keithley, 2001 multimeter). Changes in gas compositions were realized in less than 1 s at a gas flow rate of 220 mL min^{-1} with oxygen partial pressure (pO_2) range from 80 ppm to 1 atm (Table 2). A drierite laboratory gas drier was used to remove the water vapor (pH_2O calculated as 6 × 10^{-6} atm). The electrical conductivity changed continuously with the relaxation time to reach a new equilibration when the atmosphere was abruptly changed.

2.5. Determination of k_{chem} and D_{chem} by curve fitting

Based on a linearized relation between conductivity and oxygen concentration, the measured electrical conductivity is normalized and fitted to 3-dimensional diffusion equation. When the step change in oxygen partial pressure is small, the above assumption is generally legitimate [30].

$$\sigma_n = \frac{\sigma_t - \sigma_0}{\sigma_\infty - \sigma_0} \tag{1}$$

$$\sigma_n = 1 - \sum_{m=1}^{\infty}\sum_{n=1}^{\infty}\sum_{p=1}^{\infty} \frac{2L_\beta^2 exp\left(\frac{-\beta_m^2 D_{chem} t}{x^2}\right)}{\beta_m^2\left(\beta_m^2 + L_\beta^2 + L_\beta\right)} \times \frac{2L_\gamma^2 exp\left(\frac{-\gamma_n^2 D_{chem} t}{y^2}\right)}{\gamma_n^2\left(\gamma_n^2 + L_\gamma^2 + L_\gamma\right)} \times \frac{2L_\varnothing^2 exp\left(\frac{-\varnothing_p^2 D_{chem} t}{z^2}\right)}{\varnothing_p^2\left(\varnothing_p^2 + L_\varnothing^2 + L_\varnothing\right)} \tag{2}$$

$$L_\beta = x\frac{k_{chem}}{D_{chem}}; L_\gamma = y\frac{k_{chem}}{D_{chem}}; L_\varnothing = z\frac{k_{chem}}{D_{chem}} \tag{3}$$

$$\beta_m tan\beta_m = L_\beta; \gamma_n tan\gamma_n = L_\gamma; \varnothing_p tan\varnothing_p = L_\varnothing \tag{4}$$

where σ_n is normalized conductivity, σ_0 is initial conductivity, σ_∞ is final conductivity and σ_t is apparent conductivity at time t. x, y and z are dimensions of the sample, and β_m, γ_n and ϕ_p are non-zero roots of Eq. 5. The parameters L_β, L_γ, and L_ϕ correspond to the Biot number described above. Non-linear least square fitting is used to solve the diffusion equation and to obtain k_{chem} and D_{chem} from the measured relaxation curves.

3. Results and discussion

For perovskite materials, oxygen exchange with the ambient gas at high temperature occurs according to:

$$½\ O_{2,gas} + V_O^{\bullet\bullet} \leftrightarrow O_O^x + 2h^\bullet \tag{5}$$

Where O_O^x and $V_O^{\bullet\bullet}$ denote oxygen ions on the lattice sites and oxygen vacancies, respectively, and $h^\bullet$ denote electron holes. The dependence of the electrical conductivity (σ) for BCFZY0.1 on oxygen partial pressure (pO_2) is shown in Fig. 2a. At 600 °C, the conductivity increases with the increase of pO_2, suggesting a p-type electron hole conduction mechanism [31]. The total conductivity of BCFZY0.1 is about 1.6 S/cm at

Table 2
pO_2 steps applied in the ECR experiment.

logpO_2 (atm)	−4.1	−3.7	−3.0	−2.6	−2.3	−1.6	−1	−0.6778	−0.222	0
pO_2 (atm)	0.00008	0.0002	0.001	0.0025	0.005	0.025	0.1	0.21	0.6	1

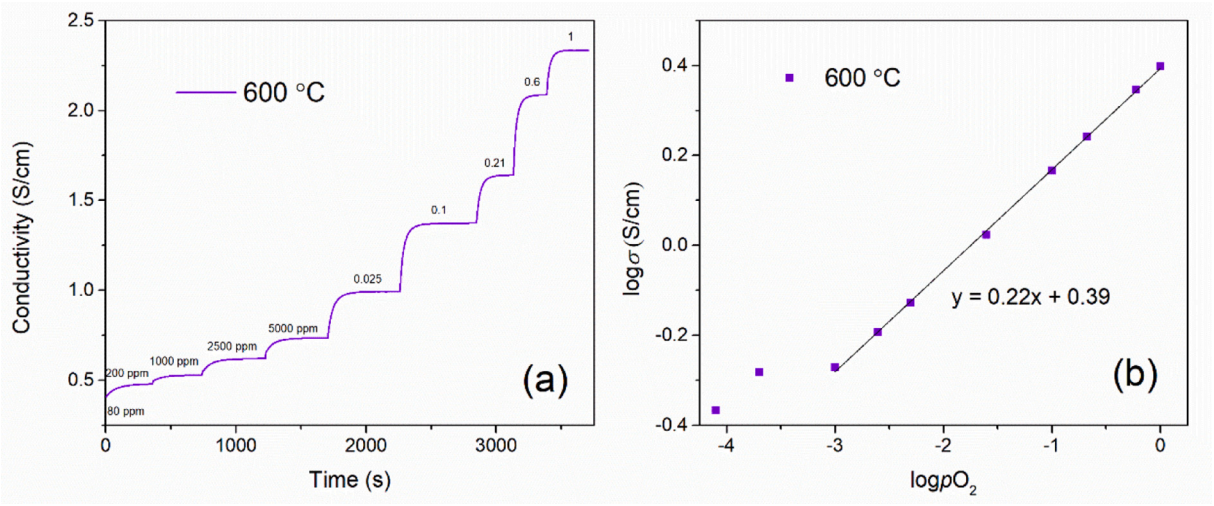

Fig. 2. (a) Oxygen partial pressure and related total conductivity changes of an BCFZY0.1 bulk sample shown as a function of time at 600 °C. (b) logarithmic plots of total electrical conductivity *versus* pO_2 for the BCFZY0.1 bar specimen at 600 °C.

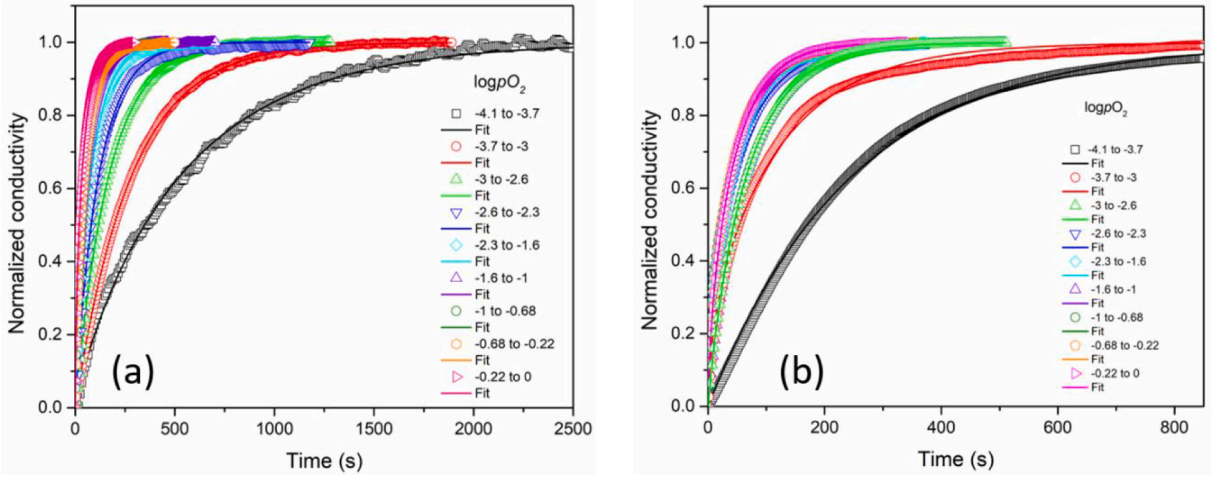

Fig. 3. The normalized conductivity relaxation curve at 600 °C for bare (a) and coated (b) BCFZY0.1 rectangular bar with different pO_2 step.

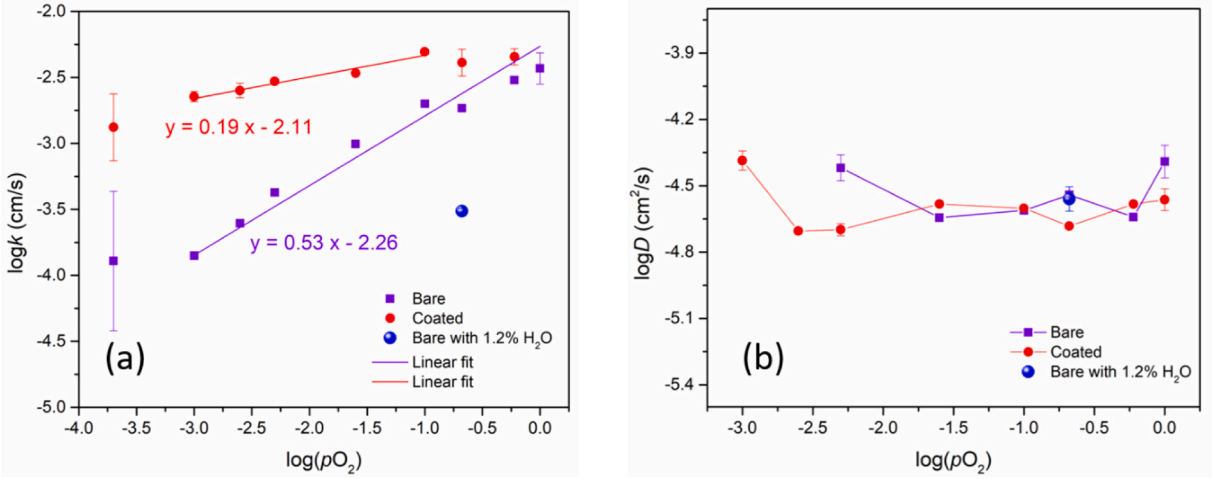

Fig. 4. Oxygen surface exchange coefficient k (a) and diffusion coefficient D (b) for bare and coated BCFZY0.1 at 600 °C as a function of oxygen partial pressure obtained from electrical conductivity relaxation.

600 °C in air, which shows much lower electrical conductivity than those of $Ba_{0.5}Sr_{0.5}Co_{0.2}Fe_{0.8}O_{3-\delta}$ (BSCF) [32–35], $La_{0.6}Sr_{0.4}Co_{0.2}Fe_{0.8}O_{3-\delta}$ (LSCF) [34]. The relatively low conductivity of BCFZY0.1 should partially ascribed to the localized 3*d* electrons in the Zr^{4+} substituted samples. [36] The total conductivity behavior is typical of many proton-conducting oxides and the character of the plot in Fig. 2b is suggested to reflect changes in the concertation of the charge carrier as a function of pO_2. [37] Under oxidizing conditions ($pO_2 > 0.001$ atm), a characteristic slope of ¼ corresponding to a *p*-type contribution can be observed [38–40]. As pO_2 decreases, loss of oxygen, thus reduction in hole-concentration tale place, decreasing hole-conductivity. At high pO_2 range, oxygen stoichiometry is higher, indicating a stronger overlap between O-2p and Co-3d orbitals which lead to a broadened valance-band for a delocalized hole-conduction [41].

Normalized conductivity curves were acquired for bare and coated BCFZY0.1 bar at 600 °C, following pO_2 step from 80 ppm to 1 atm are shown in Fig. 3. In the conductivity relaxation experiments of bare sample (Fig. 3a), the times needed to re-equilibrate the sample were seen to increase strongly at low pO_2. For example, the relaxation time is ~200 s with log pO_2 step change from −0.22 to 0, while it increases to ~2500 when logpO_2 step change from −4.1 to −3.7. In general, the rate of re-equilibration may be affected by slow surface exchange and bulk diffusion. Specifically, at low pO_2 range, the diffusion coefficient could no longer be determined due to the limitation of low surface oxygen exchange rate [42]. In order to determine both surface exchange coefficient (*k*) and diffusion coefficient (*D*) in a wide range of pO_2, a porous BCFZY0.1 layer was coated on the bar to increase the effective surface area on which exchange of oxygen may occur. As can be seen from Fig. 3b, after the porous layer was coated on the surface of the specimen, the relaxation time decreased significantly, indicating that the coated porous layer accelerated the kinetics of oxygen exchange. The strong relaxation time dependence of pO_2 may indicate that the rate-determining step in the exchange process involves molecular oxygen.

Normalized conductivity relaxation curves were fitted using the diffusion equations to determine k_{chem} and D_{chem} values, assuming that the oxygen transport reaction is dominated by both surface exchange and bulk diffusion processes This assumption has been known to be valid when the thickness of the sample is close to its characteristic thickness. [30,35] Fig. 4 shows that values of *k* and *D* for each of the samples obtained from fitting. The result in Fig. 4a shows that the value of *k* of BCFZY0.1 are significantly affected by the surface coating (error bars are smaller than the symbol size for some data). *k* is found to increase upon coating with porous layer, up to a factor of ~4 after coating with a porous layer compared to bare BCFZY0.1. This observation can be tentatively explained by the increase of surface area and associated sites involved in the oxygen exchange reaction [43,44].

As defined by Bouwmeester [45], the ratio of *D* to *k* has been defined as characteristic thickness (L_c) and was used to qualitatively describe the relative control of transport, either by surface exchange or bulk diffusion. Lie et al. proposed normalize L_c by membrane thickness *d*, [24].

$$L = \frac{d}{L_c} = \frac{dk}{D} \tag{6}$$

Of $0.1 < L < 10$, the oxygen transport process should be considered as a mixed control process. Fig. S3 shows the characteristic thickness of BCFZY0.1 as a function of pO_2 at 600 °C. The critical length scale, L_c, is

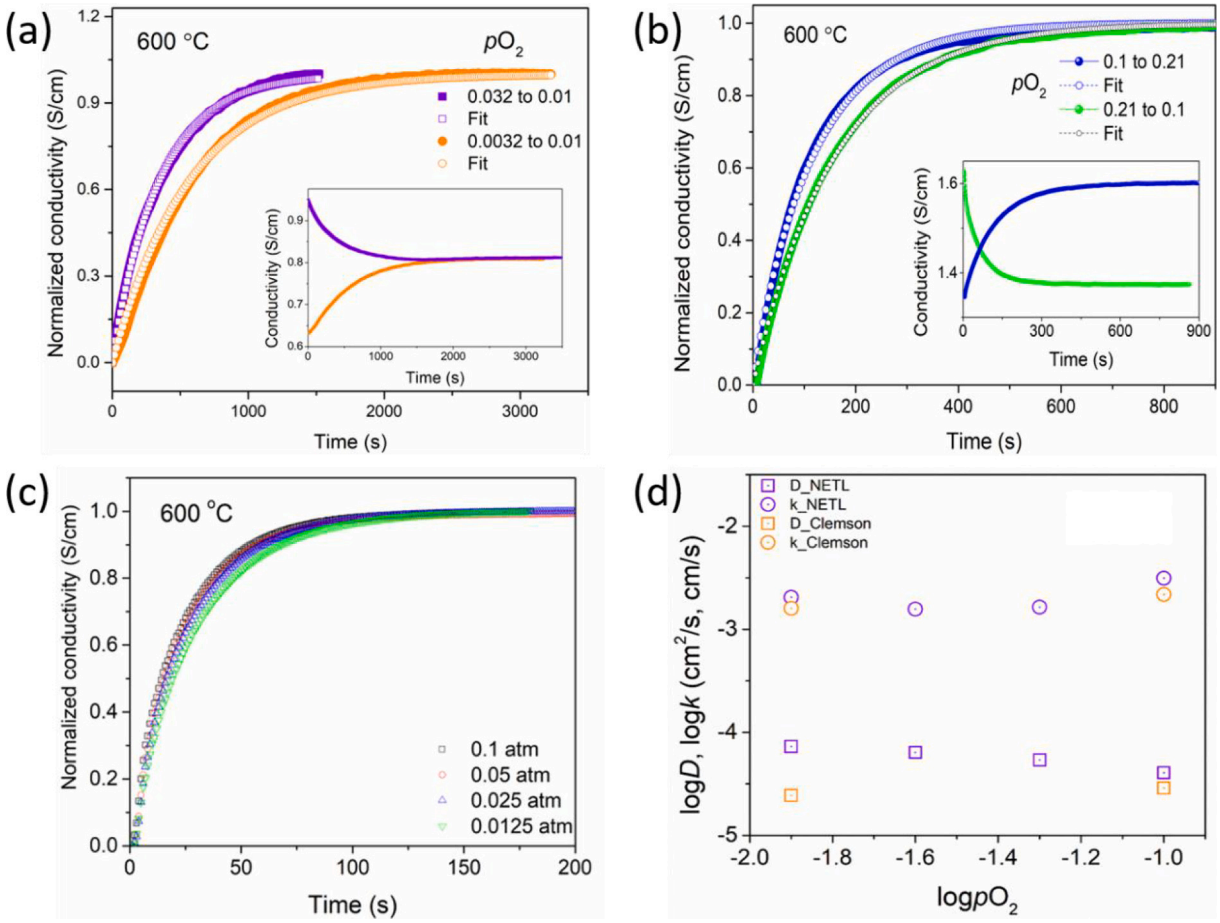

Fig. 5. Comparison of the ECR profile of BCFZY0.1 under oxidation and reduction processes with a fixed final pO_2 (a), comparison of ECR profile of BCFZY0.1 with pO_2 from low to high (0.025 to 0.1 atm) and high to low (0.21 to 0.1) (b), the normalized conductivity at 600 °C along with the elapsed time measured by NETL by switching the gas from high to low pO_2 (c), comparison of *k* and *D* obtained by NETL and Clemson at 600 °C (d).

found to be in the range $75 < L_c < 230$ μm when pO_2 ranges from 0.025 to 1 atm, which is very close to the L_c of LSCF (30 to 300 μm) [46]. When normalized by the thickness, L, the Lc value for the 1.12 mm thick bar is found to be between 0.1 and 10, indicating that the relaxation behavior is under mixed control from both diffusion and surface exchange processes under the applied experimental conditions. Fig. 4b shows that the D extracted from bare and coated samples are in quantitative agreement, indicating that the applied pO_2 step size is small enough to assume a constant value of D during the re-equilibration. The present observations confirmed the general expectation that the oxygen diffusivity in BCFZY0.1 is not affected by surface coating. In addition, we compared the fitted kinetic parameters obtained from ECR performed by multiple independent partners NETL and Clemson, respectively in this work. NETL conducted the ECR experiment by switching the gas from high to low pO_2 and the relaxation profile is shown in Fig. 5a. According to the normalized relaxation profile, with a fixed final pO_2, a hysteresis behavior with the oxidation process (low to high pO_2, Clemson) requiring more equilibration time than the reduction process (high to low pO_2, NETL). After fitting, the result shows that both k and D obtained from Clemson have a smaller value compared to that from NETL (Fig. 5d). When comparing the ECR profile of with same pO_2 changing step (0.1 to 0.21 atm), longer equilibration time is required when pO_2 was changed from a lower pO_2. That is because the oxygen surface exchange coefficient mainly depends on final pO_2, which is consistent with the findings demonstrated by Li et al. [24] Yoo et al. reported that k is a function of $pO_2{}^n$. [47] Therefore, a higher final pO_2 leads to shorter relaxation time and thus a higher k value.

Fig. 6 presents the 2-D contour plots of fitting error of k and D obtained for bare BCFZY0.1 bar under 0.0025 to 0.005 atm. Here, Euclidean norm, also known as L2-norm, was used. The L2-norm of the difference between the target data and the calculated data was obtained for the specific set of k & D value. The plots of the norms for all the possible sets of k& D values in 2-D domain show the distribution of the fitting error and the quality of the fitting function. The blue colored area in Fig. 6b particularly indicates a confidence region with 1% tolerance, showing most reliable k and D values. Thus, the contour plots provide intuitive presentation of the relative reliability of k and D values.

Table 3 compares the of oxygen surface exchange coefficient k and diffusion coefficient D of BCFZY0.1 with typical MIEC materials in the literature. The surface exchange coefficient k of BCFZY0.1 is higher than that of LSCF, LSC and SF, while the diffusion coefficient D is two orders of magnitude higher than BSCF at 600° C. This observation indicates BCFZY0.1 can act as a good oxygen conductor.

In order to further access the electrochemical property of BCFZY0.1 as cathode material, impedance data of BCFZY0.1 | BCZYSm13 | BCFZY0.1 symmetric cell was measured in wet air at temperature range from 550 °C to 700 °C (Fig. 7). The ASR decreases as temperature increases. At 600 °C, BCFZY0.1 has an area specific resistance (ASR) value about 0.9 Ω cm^2, and the corresponding activation energy calculated from ASR plot was about 1.12 eV.

Table 3
Comparison of oxygen surface exchange coefficient k and diffusion coefficient D of BCFZY0.1 with materials in the literature.

Materials	Temperature (°C)	pO_2 (atm)	k (cm s^{-1})	D (cm^2/s)	Reference
LSCF	800	0.2	1.2×10^{-4}	8.0×10^{-6}	[24]
PSCF	900	0.073	3.98×10^{-4}	9.7×10^{-5}	[35]
BSCF	600	0.2	8.1×10^{-7}	3.0×10^{-7}	[48]
BSF	600	0.5	1.1×10^{-6}	6.1×10^{-7}	[48]
SF	600	0.5	7.6×10^{-9}	2.3×10^{-8}	[48]
SDC	800	0.2	2.3×10^{-4}		[49]
LSC	800	0.2	3.4×10^{-4}	2.5×10^{-5}	[49]
This work	600	0.21	1.85×10^{-3}	2.9×10^{-5}	

Single cell BCZYSm13 + 60% NiO | BCZYSm13 | BCFZY0.1 were prepared using the route described in Fig. 1. The microstructure of the fractured cross section and of the as-sintered single cell are presented in Fig. 8. The electrolyte layer has a thickness of approximately 25 μm. The BCFZY0.1 cathode was porous with a nano-scale grain size (Fig. 8 b). The as-prepared electrochemical cell was tested in fuel cell mode of operation. The maximum power density of the cell (P_{max}) reached ~200 mW/cm^2 at 600 °C and the corresponding impedance spectroscopy results are displayed. The ohmic resistance was found to be ~0.58 Ω cm^2 and the polarization resistance was ~0.85 Ω cm^2 at 600 °C under OCV condition. The enhancement of power output can be realized by reducing the electrolyte thickness and minimizing ohmic losses along with associated reduction in electrode polarization resistance. Furthermore, the R_p occupies 59% of the total ASR of the single cell, which is responsible for the main resistance during the operation. Typically, the PCFC cathode performance is strongly dependent on the cathode morphologies. R_p can be further improved by optimize the microstructure of the cathode by introducing pore formers, changing preparation temperatures or infiltration of active oxygen reduction catalysts.

In order to simulate the real working condition of the cathode in the fuel cell mode, ECR experiment was conducted with introducing H_2O into the ECR chamber. The H_2O content was calculated to be around 1.2% according to the peak current density at 600 °C. As shown in Fig. 4a, surface exchange rate of oxygen decreased from 1.85×10^{-3} cm

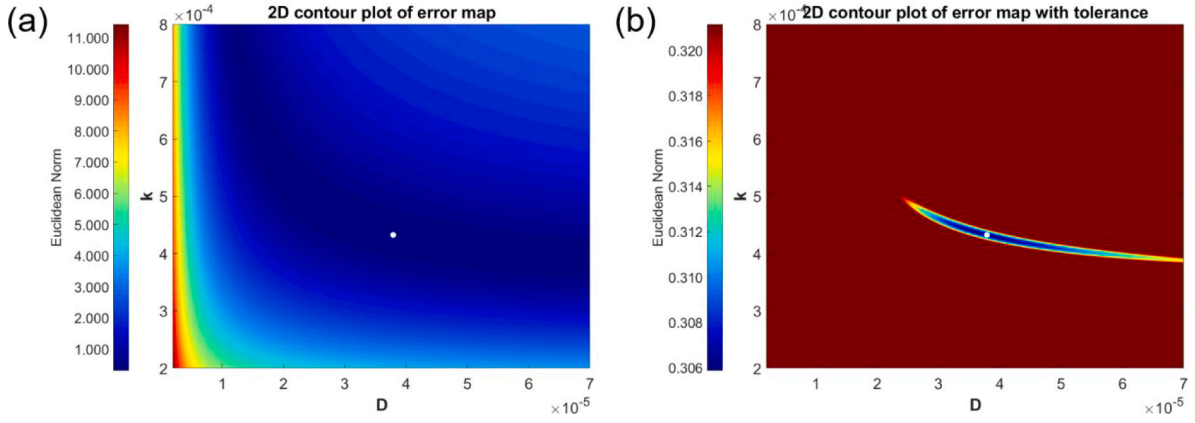

Fig. 6. Fitting error color maps for bare BCFZY0.1 bar under 0.0025 to 0.005 atm.

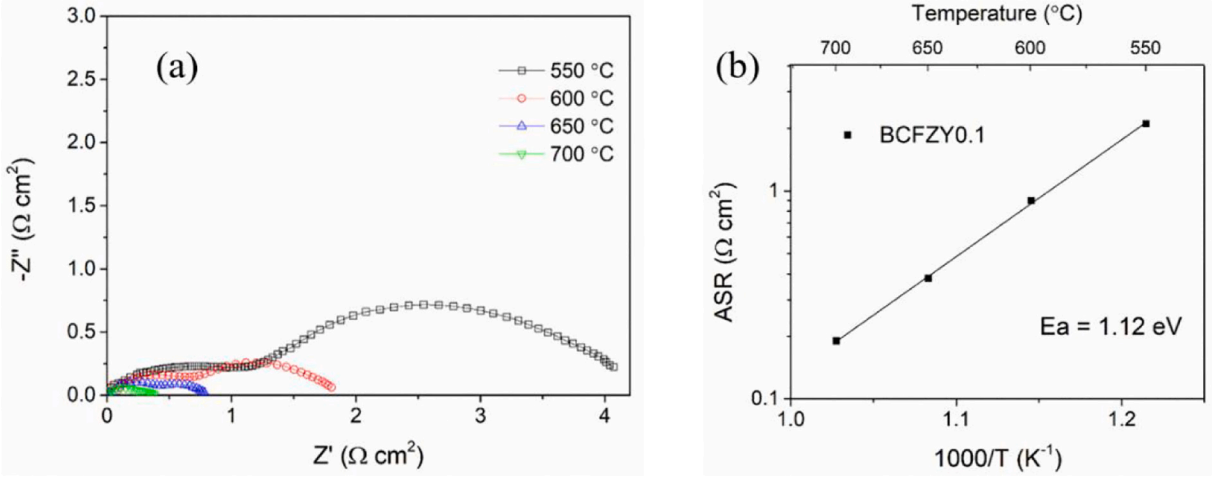

Fig. 7. EIS of BCFZY0.1 | BCZYSm13 | BCFZY0.1 symmetric cell measured in wet air (a), Arrhenius diagram as a function of temperature (b).

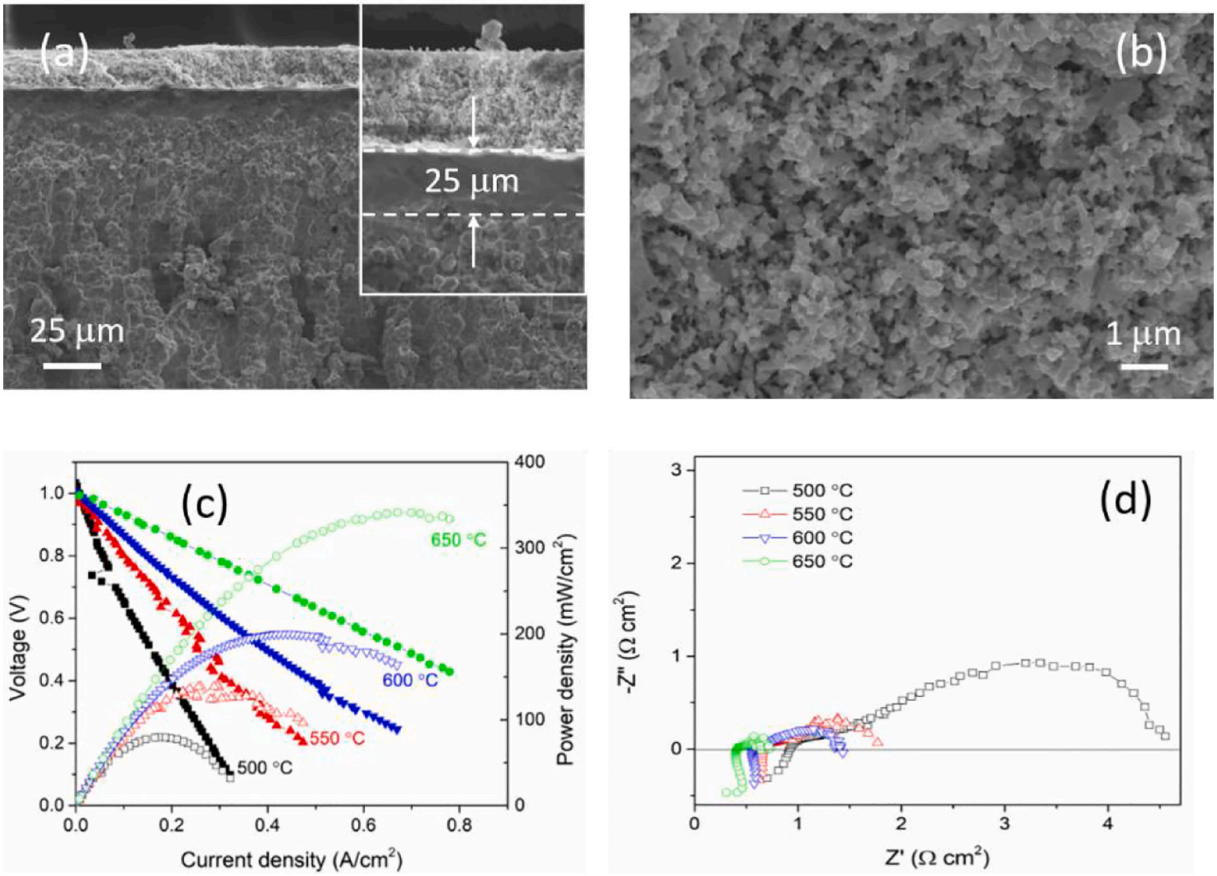

Fig. 8. (a) SEM images of BCZYSm13 + 60% NiO | BCZYSm13 | BCFZY single cell, (b) enlarged view of BCFZY0.1 cathode. (c) I-V curves and corresponding power densities measured at temperature range between 450 and 650 °C under H_2/ air, and (d) impedance spectra of single cells measured under OCV condition.

s^{-1} to 3.06 × 10^{-4} cm s^{-1} when 1.2% H_2O was introduced while diffusion coefficient keeps a constant, which indicate that adsorption of H_2O would suppress the oxygen exchange rate. The incorporation of proton would increase the proton concentration and thus reduces hole concentration as well as the electrical conductivity according to Eq. (7).

$$H_2O + 2O_O^{\times} + 2h^{\bullet} \leftrightarrow 2OH_O^{\bullet} + \frac{1}{2}O_2 \quad (7)$$

This statement is also confirmed by a decrease in the conductivity with the presence of H_2O as shown in Fig. S5. As suggested by Shimojo el al., [50], oxygen vacancies on the surface, which is active site for oxygen exchange, are also influential for the dissociative adsorption of H_2O molecules. Therefore, the competitive adsorption relationship between oxygen and H_2O may account for the decrease of surface exchange coefficient in the presence of H_2O.

4. Conclusions

In this work, data of ECR experiment have been presented on dense

BCFZY0.1 ceramic either bare or coated with a porous layer on the surface. Surface exchange coefficient k and diffusion coefficient D was obtained by fitting the relaxation curve under different pO_2 steps. The results show that application of a porous layer on the surface of BZCFZY0.1 represents attractive approach for improving the ORR kinetics. The competitive adsorption relationship between oxygen and H_2O leads to a decrease of exchange kinetics in the presence of H_2O. A phase inversion tape casting method was used to prepare a porous anode. Configuration of 40 wt% BCZYSm13 + 60 wt% NiO | BCZYSm13 | BCFZY0.1 cell exhibits a power density of ~200 mW/cm^2 at 600 °C. The single cell performance can be further improved by optimizing the microstructure of the cathode through the introduction of pore formers or changing preparation temperatures.

Declaration of Competing Interest

The authors declare that they have no known competing financial interests or personal relationships that could have appeared to influence the work reported in this paper.

Acknowledgments

This project was funded by the Department of Energy, National Energy Technology Laboratory an agency of the United States Government, through an appointment administered by the Oak Ridge Institute for Science and Education. Neither the United States Government nor any agency thereof, nor any of its employees, nor the support contractor, nor any of their employees, makes any warranty, express or implied, or assumes any legal liability or responsibility for the accuracy, completeness, or usefulness of any information, apparatus, product, or process disclosed, or represents that its use would not infringe privately owned rights. Reference herein to any specific commercial product, process, or service by trade name, trademark, manufacturer, or otherwise does not necessarily constitute or imply its endorsement, recommendation, or favoring by the United States Government or any agency thereof. The views and opinions of authors expressed herein do not necessarily state or reflect those of the United States Government or any agency thereof.

Appendix A. Supplementary data

Supplementary data to this article can be found online at https://doi.org/10.1016/j.ssi.2021.115639.

References

[1] C. Duan, J. Tong, M. Shang, S. Nikodemski, M. Sanders, S. Ricote, A. Almansoori, R. O'Hayre, Readily processed protonic ceramic fuel cells with high performance at low temperatures, Science. 349 (2015) 1321–1326, https://doi.org/10.1126/science.aab3987.

[2] A.R. Hanifi, N.K. Sandhu, T.H. Etsell, J.-L. Luo, P. Sarkar, Fabrication and characterization of a tubular ceramic fuel cell based on $BaZr_{0.1}Ce_{0.7}Y_{0.1}Yb_{0.1}O_{3-\delta}$ proton conducting electrolyte, Journal of Power Sources 341 (2017) 264–269, https://doi.org/10.1016/j.jpowsour.2016.12.010.

[3] L. Yang, S. Wang, K. Blinn, M. Liu, Z. Liu, Z. Cheng, M. Liu, Enhanced sulfur and coking tolerance of a mixed ion conductor for SOFCs: $BaZr_{0.1}Ce_{0.7}Y_{0.2-x}Yb_xO_{3-\delta}$, Science 326 (2009) 126–129, https://doi.org/10.1126/science.1174811.

[4] Y. Ling, J. Yu, B. Lin, X. Zhang, L. Zhao, X. Liu, a cobalt-free $Sm_{0.5}Sr_{0.5}Fe_{0.8}Cu_{0.2}O_{3-\delta}$–$Ce_{0.8}Sm_{0.2}O_{2-\delta}$ composite cathode for proton-conducting solid oxide fuel cells, J. Power Sources 196 (2011) 2631–2634, https://doi.org/10.1016/j.jpowsour.2010.11.017.

[5] Y. Yoo, N. Lim, Performance and stability of proton conducting solid oxide fuel cells based on yttrium-doped barium cerate-zirconate thin-film electrolyte, J. Power Sources 229 (2013) 48–57, https://doi.org/10.1016/j.jpowsour.2012.11.094.

[6] S. Sun, Z. Cheng, Effects of H_2O and CO_2 on electrochemical behaviors of BSCF cathode for proton conducting IT-SOFC, J. Electrochem. Soc. 164 (2017) F81–F88, https://doi.org/10.1149/2.0611702jes.

[7] J.W. Fergus, Electrolytes for solid oxide fuel cells, J. Power Sources 162 (2006) 30–40, https://doi.org/10.1016/j.jpowsour.2006.06.062.

[8] M. Liu, J. Gao, X. Liu, G. Meng, High performance of anode supported $BaZr_{0.1}Ce_{0.7}Y_{0.2}O_{3-\delta}$(BZCY) electrolyte cell for IT-SOFC, International Journal of Hydrogen Energy 36 (2011) 13741–13745, https://doi.org/10.1016/j.ijhydene.2011.07.087.

[9] B. Wang, L. Bi, X.S. Zhao, Exploring the role of NiO as a sintering aid in $BaZr_{0.1}Ce_{0.7}Y_{0.2}O_{3-\delta}$ electrolyte for proton-conducting solid oxide fuel cells, Journal of Power Sources 399 (2018) 207–214, https://doi.org/10.1016/j.jpowsour.2018.07.087.

[10] Y. Meng, J. Gao, H. Huang, M. Zou, J. Duffy, J. Tong, K.S. Brinkman, A high-performance reversible protonic ceramic electrochemical cell based on a novel Sm-doped $BaCe_{0.7}Zr_{0.1}Y_{0.2}O_{3-\delta}$ electrolyte, J. Power Sources 439 (2019) 227093, https://doi.org/10.1016/j.jpowsour.2019.227093.

[11] B. Wang, L. Bi, X.S. Zhao, Liquid-phase synthesis of $SrCo_{0.9}Nb_{0.1}O_{3-\delta}$ cathode material for proton-conducting solid oxide fuel cells, Ceramics International 44 (2018) 5139–5144, https://doi.org/10.1016/j.ceramint.2017.12.116.

[12] Y. Chen, T. Hong, P. Wang, K. Brinkman, J. Tong, J. Cheng, Investigate the proton uptake process of proton/oxygen ion/hole triple conductor $BaCo_{0.4}Fe_{0.4}Zr_{0.1}Y_{0.1}O_{3-\delta}$ by electrical conductivity relaxation, J. Power Sources 440 (2019) 227122, https://doi.org/10.1016/j.jpowsour.2019.227122.

[13] R. Zohourian, R. Merkle, G. Raimondi, J. Maier, Mixed-conducting Perovskites as cathode materials for Protonic ceramic fuel cells: understanding the trends in proton uptake, Adv. Funct. Mater. 28 (2018) 1801241, https://doi.org/10.1002/adfm.201801241.

[14] R. Ren, Z. Wang, C. Xu, W. Sun, J. Qiao, D.W. Rooney, K. Sun, Tuning the defects of the triple conducting oxide $BaCo_{0.4}Fe_{0.4}Zr_{0.1}Y_{0.1}O_{3-\delta}$ perovskite toward enhanced cathode activity of protonic ceramic fuel cells, Journal of Materials Chemistry A 7 (2019) 18365–18372. https://doi.org/10.1039/C9TA04335G.

[15] X. Kuai, G. Yang, Y. Chen, H. Sun, J. Dai, Y. Song, R. Ran, W. Wang, W. Zhou, Z. Shao, Boosting the activity of $BaCo_{0.4}Fe_{0.4}Zr_{0.1}Y_{0.1}O_{3-\delta}$ perovskite for oxygen reduction reactions at low-to-intermediate temperatures through tuning b-site cation deficiency, Advanced Energy Materials 9 (2019) 1902384, https://doi.org/10.1002/aenm.201902384.

[16] X. Li, L. He, X. Zhong, J. Zhang, S. Luo, W. Yi, L. Zhang, M. Hu, J. Tang, X. Zhou, X. Zhao, B. Xu, Evaluation of A-site Ba $^{2+}$ -deficient $Ba_{1-x}co_{0.4}Fe_{0.4}Zr_{0.1}Y_{0.1}O_{3-\delta}$ oxides as Electrocatalysts for efficient hydrogen evolution reaction, Scanning. 2018 (2018) 1–10, https://doi.org/10.1155/2018/1341608.

[17] H. Qi, Z. Zhao, B. Tu, M. Cheng, Reaction tuned formation of hierarchical $BaCo_{0.4}Fe_{0.4}Zr_{0.1}Y_{0.1}O_{3-\delta}$ cathode, Journal of Power Sources 455 (2020) 227971, https://doi.org/10.1016/j.jpowsour.2020.227971.

[18] T. Hong, M. Zhao, K. Brinkman, F. Chen, C. Xia, Enhanced Oxygen Reduction activity on ruddlesden–popper phase decorated $La_{0.8}Sr_{0.2}FeO_{3-\delta}$ 3D Heterostructured cathode for solid oxide fuel cells, ACS Appl. Mater. Interfaces 9 (2017) 8659–8668, https://doi.org/10.1021/acsami.6b14625.

[19] B. Hu, C. Xia, Factors influencing the measured surface reaction kinetics parameters: factors influencing the measured surface reaction kinetics parameters, Asia Pac. J. Chem. Eng. 11 (2016) 327–337, https://doi.org/10.1002/apj.1993.

[20] S. Zhu, D. Ding, M. Li, C. Xia, Effect of Samaria doped ceria impregnation on the electrochemical performance of strontium doped lanthanum chromium manganite anode for solid oxide fuel cells, J. Electrochem. Soc. 164 (2017) F916–F922, https://doi.org/10.1149/2.0591709jes.

[21] B. Hu, K. Guo, M. Li, Y. Li, C. Xia, Effect of SDC grain size on the oxygen incorporation at the LSCF-SDC-gas three-phase boundary, J. Electrochem. Soc. 163 (2016) F190–F195, https://doi.org/10.1149/2.0441603jes.

[22] S. Saher, S. Naqash, B.A. Boukamp, B. Hu, C. Xia, H.J.M. Bouwmeester, Influence of ionic conductivity of the nano-particulate coating phase on oxygen surface exchange of $La_{0.58}Sr_{0.4}Co_{0.2}Fe_{0.8}O_{3-\delta}$, J. Mater. Chem. A 5 (2017) 4991–4999. https://doi.org/10.1039/C6TA10954C.

[23] Y. Meng, L. Sun, J. Gao, W. Tan, C. Chen, J. Yi, H.J.M. Bouwmeester, Z. Sun, K. S. Brinkman, Insights into the CO_2 stability-performance trade-off of antimony-doped $SrFeO_{3-\delta}$ Perovskite cathode for solid oxide fuel cells, ACS Appl. Mater. Interfaces 11 (2019) 11498–11506, https://doi.org/10.1021/acsami.9b00876.

[24] Y. Li, K. Gerdes, T. Horita, X. Liu, Surface exchange and bulk diffusivity of LSCF as SOFC cathode: electrical conductivity relaxation and isotope exchange characterizations, J. Electrochem. Soc. 160 (2013) F343–F350, https://doi.org/10.1149/2.044304jes.

[25] Y. Li, K. Gerdes, H. Diamond, X. Liu, An improved method to increase the predictive accuracy of the ECR technique, Solid State Ionics 204–205 (2011) 104–110, https://doi.org/10.1016/j.ssi.2011.09.017.

[26] J.A. Lane, J.A. Kilner, Measuring oxygen diffusion and oxygen surface exchange by conductivity relaxation, Solid State Ionics 136–137 (2000) 997–1001, https://doi.org/10.1016/S0167-2738(00)00554-3.

[27] J. Tong, D. Clark, M. Hoban, R. O'Hayre, Cost-effective solid-state reactive sintering method for high conductivity proton conducting yttrium-doped barium zirconium ceramics, Solid State Ionics 181 (2010) 496–503, https://doi.org/10.1016/j.ssi.2010.02.008.

[28] J. Tong, D. Clark, L. Bernau, A. Subramaniyan, R. O'Hayre, Proton-conducting yttrium-doped barium cerate ceramics synthesized by a cost-effective solid-state reactive sintering method, Solid State Ionics 181 (2010) 1486–1498, https://doi.org/10.1016/j.ssi.2010.08.022.

[29] J. Gao, Y. Meng, T. Hong, S. Kim, S. Lee, K. He, K.S. Brinkman, Rational anode design for protonic ceramic fuel cells by a one-step phase inversion method, J. Power Sources 418 (2019) 162–166, https://doi.org/10.1016/j.jpowsour.2019.02.040.

[30] H.J.M. Bouwmeester, M.W. Den Otter, B.A. Boukamp, Oxygen transport in $La_{0.6}Sr_{0.4}Co_{1-y}Fe_yO_{3-\delta}$, J Solid State Electrochem 8 (2004) 599–605, https://doi.org/10.1007/s10008-003-0488-3.

[31] L. Jiang, J. Wang, X. Xiong, X. Jin, Q. Pei, K. Huang, Thermal and electrical stability of $Sr_{0.9}Y_{0.1}CoO_{2.5+\delta}$ as a promising cathode for intermediate-temperature

solid oxide fuel cells, J. Electrochem. Soc. 163 (2016) F330–F335, https://doi.org/10.1149/2.0361605jes.
[32] S.M. Fang, C.-Y. Yoo, H.J.M. Bouwmeester, Performance and stability of niobium-substituted $Ba_{0.5}Sr_{0.5}Co_{0.8}Fe_{0.2}O_{3-\delta}$ membranes, Solid State Ionics 195 (2011) 1–6, https://doi.org/10.1016/j.ssi.2011.05.022.
[33] B. Wei, Z. Lü, X. Huang, J. Miao, X. Sha, X. Xin, W. Su, Crystal structure, thermal expansion and electrical conductivity of perovskite oxides $Ba_xSr_{1-x}Co_{0.8}Fe_{0.2}O_{3-\delta}$ ($0.3\leq x\leq 0.7$), J. Eur. Ceram. Soc. 26 (2006) 2827–2832, https://doi.org/10.1016/j.jeurceramsoc.2005.06.047.
[34] D. Rembelski, J.P. Viricelle, L. Combemale, M. Rieu, Characterization and comparison of different cathode materials for SC-SOFC: LSM, BSCF, SSC, and LSCF, Fuel Cells 12 (2012) 256–264, https://doi.org/10.1002/fuce.201100064.
[35] C. Niedrig, S.F. Wagner, W. Menesklou, S. Baumann, E. Ivers-Tiffée, Oxygen equilibration kinetics of mixed-conducting perovskites BSCF, LSCF, and PSCF at 900 °C determined by electrical conductivity relaxation, Solid State Ionics 283 (2015) 30–37, https://doi.org/10.1016/j.ssi.2015.11.004.
[36] G. Kaur, Intermediate Temperature Solid Oxide Fuel Cells: Electrolytes, Electrodes and Interconnects, Elsevier, 2019.
[37] M. Chen, S. Paulson, W.H. Kan, V. Thangadurai, V. Birss, Surface and bulk study of strontium-rich chromium ferrite oxide as a robust solid oxide fuel cell cathode, J. Mater. Chem. A 3 (2015) 22614–22626, https://doi.org/10.1039/C5TA05815E.
[38] D.-K. Lim, H.-N. Im, S.-Y. Jeon, J.-Y. Park, S.-J. Song, Experimental evidence of hydrogen–oxygen decoupled diffusion into $BaZr_{0.6}Ce_{0.25}Y_{0.15}O_{3-\delta}$, Acta Materialia 61 (2013) 1274–1283, https://doi.org/10.1016/j.actamat.2012.11.003.
[39] D.-K. Lim, M.-B. Choi, K.-T. Lee, H.-S. Yoon, E.D. Wachsman, S.-J. Song, Non-monotonic conductivity relaxation of proton-conducting $BaCe_{0.85}Y_{0.15}O_{3-\delta}$ upon hydration and dehydration, International Journal of Hydrogen Energy 36 (2011) 9367–9373, https://doi.org/10.1016/j.ijhydene.2011.04.203.
[40] Ivanov Tsvetkov, Sereda Malyshkin, Zuev, Thermoelectric Behavior of $BaZr_{0.9}Y_{0.1}O_{3-d}$ Proton Conducting Electrolyte, Membranes 9 (2019) 120, https://doi.org/10.3390/membranes9090120.
[41] J. Wang, T. Yang, L. Lei, K. Huang, Ta-doped $SrCoO_{3-\delta}$ as a promising bifunctional oxygen electrode for reversible solid oxide fuel cells: a focused study on stability, J. Mater. Chem. A 5 (2017) 8989–9002, https://doi.org/10.1039/C7TA02003A.
[42] J.E. ten Elshof, M.H.R. Lankhorst, H.J.M. Bouwmeester, Chemical diffusion and oxygen exchange of $La_{0.6}Sr_{0.4}Co_{0.6}Fe_{0.4}O_{3-d}$, Solid State Ionics 99 (1997) 15–22.
[43] Ganeshananthan Ramannan, A. Virkar, Measurement of surface exchange coefficient on pporous $La_{0.6}Sr_{0.4}CoO_{3-d}$ sample by conductivity relaxation, Journal of The Electrochemical Society 152 (2005) A1620–A1628, https://doi.org/10.1149/1.1940828.
[44] P. Hjalmarsson, M. Søgaard, M. Mogensen, Oxygen transport properties of dense and porous $(La_{0.8}Sr_{0.2})_{0.99}Co_{0.8}Ni_{0.2}O_{3-\delta}$, Solid State Ionics 180 (2009) 1290–1297, https://doi.org/10.1016/j.ssi.2009.07.012.
[45] C.H. Chen, H.J.M. Bouwmeester, Oxygen permeation of $La_{0.3}Sr_{0.7}CoO_{3-d}$, Solid State Ionics 98 (1997) 7–13.
[46] S. Saher, S. Naqash, B.A. Boukamp, B. Hu, C. Xia, H.J.M. Bouwmeester, Influence of ionic conductivity of the nano-particulate coating phase on oxygen surface exchange of $La_{0.58}Sr_{0.4}Co_{0.2}Fe_{0.8}O_{3-\delta}$, J. Mater. Chem. A 5 (2017) 4991–4999. https://doi.org/10.1039/C6TA10954C.
[47] C.-Y. Yoo, H.J.M. Bouwmeester, Oxygen surface exchange kinetics of $SrTi_{1-x}Fe_xO_{3-\delta}$ mixed conducting oxides, Phys. Chem. Chem. Phys. 14 (2012) 11759–11765, https://doi.org/10.1039/C2CP41923H.
[48] L. Wang, R. Merkle, J. Maier, Surface kinetics and mechanism of oxygen incorporation into $Ba_{1-x}Sr_xCo_yFe_{1-y}O_{3-\delta}$ SOFC microelectrodes, J. Electrochem. Soc. 157 (2010) B1802, https://doi.org/10.1149/1.3494224.
[49] Y. Li, Oxygen Transport Kinetics in Solid Oxide Fuel Cell Cathode, PhD, West Virginia University Libraries, 2012, https://doi.org/10.33915/etd.4887.
[50] F. Shimojo, Ab initio study of proton dynamics on perovskite oxide surfaces, Sci. Technol. Adv. Mater. 8 (2007) 504–510, https://doi.org/10.1016/j.stam.2007.08.004.